

Peculiarity of convergence of shock wave generated by underwater electrical explosion of ring-shaped wire

D. Shafer, G. R. Toker, V. Tz. Gurovich, S. Gleizer, and Ya. E. Krasik
 Physics Department, Technion, Haifa 32000, Israel

(Received 21 February 2013; accepted 24 April 2013; published online 8 May 2013)

Nanosecond timescale underwater electrical wire explosions of ring-shaped Cu wires were investigated using a pulsed generator with a current amplitude up to 50 kA. It was shown that this type of wire explosion results in the generation of a toroidal shock wave (SW). Time- and space-resolved optical diagnostics were used to determine azimuthal uniformity of the shock wave front and its velocity. It was found that the shock wave preserves its circular front shape in the range of radii $50 \mu\text{m} < r < 5 \text{ mm}$. At $r \leq 15 \mu\text{m}$, azimuthal irregularities of the SW front were obtained indicating the appearance of azimuthal instability. A surprising finding is that the shock wave propagates with a constant velocity of $v_{sw} = 1.2M$, where M is the Mach number. The dynamics of the leading part of the shock wave, based on the oblique shock wave theory, is presented, explaining the constant velocity of the shock wave. © 2013 AIP Publishing LLC. [<http://dx.doi.org/10.1063/1.4804342>]

I. INTRODUCTION

The cumulation of energy in a small and confined space, where the energy density (and other thermodynamic parameters) rises and reaches high values near the axis or point of implosion, is a subject of a great interest in science. There are several well-known examples of cumulative processes, for instance, converging shock waves (SW) in different media, the collapse of an air-filled bubble in water, and electromagnetic SW.¹ It is well known that the amplitude of a converging SW with a spherically or cylindrically symmetric front is amplified by the $A^2 \sim S^{-1}$ law, where A is the amplitude and S is the area of the surface of the SW. The above statement is merely a result of the conservation of energy: as the SW converges, the energy that it carries along is being confined into a smaller volume and distributed over a decreasing SW front area. For example,² in a weak SW propagating in an ideal gas, the temperature rises as $T(r) \sim r^{-1}$, while in a cylindrical case $T(r) \sim r^{-0.5}$. In the experimental perspective, the convergence of the SW results in the finite cumulation of energy, i.e., in the growth of the pressure behind the SW front in the vicinity of its point of implosion.

In general, the parameters of the converging SW depend on the properties of the source that generated it. However, at a certain point of convergence, the SW “forgets” how it was created³ and starts to behave self-similarly, i.e., the process of cumulation can be described by a self-similar solution of the hydrodynamic equations.⁴ Such self-similar solutions were first found by Guderley,⁵ and later independently by Landau⁶ and Stanykovich,⁷ when they considered a converging cylindrical or spherical SW propagating in an ideal gas. For this problem, self-similarity solutions were found for different gas adiabatic coefficients $\gamma = 3$ (Stanykovich and Landau⁶) and $\gamma = 1.4$ (Guderley⁵); the resulting temperature dependencies on radius were $T \sim r^{-1.14}$ and $T \sim r^{-0.79}$, respectively, and the shock wave’s front pressure was approaching infinity for both solutions, while the density remained finite at the point of implosion. Let us note that at the present there is no complete answer about the range of

applicability and, respectively, the correctness of solutions for the limit of cumulation of strong shock waves (SSWs). For instance, in a review,² different models of instabilities were considered, including models showing that, in the case of water, the converging SW is stable even in linear approximation, and small perturbations do not limit the cumulation. Therefore, for each experiment, this limit should be determined independently.

The convergence of toroidal SWs in air at different pressures has been investigated by Berezhetskaya *et al.*⁸ A significant increase in the pressure near the point of convergence was found, since air is not a dense material, its compressibility is high, and its equation-of-state (EOS) fits well with that of an ideal gas. Water, in contrast to air, is very difficult to compress, and similarly to air it allows optical observation. Therefore, it is very interesting to perform SW implosion experiments in water and investigate the behavior of the toroidal SW front near the axis or point of implosion. Underwater electrical wire explosion is a convenient method of generating SW in water. The water environment prevents surface flashover and fast wire expansion, which allows high energy density deposition to be achieved.^{9,10} It was shown that up to 90% of the stored energy can be deposited into the exploding wire, which generates a uniform cylindrical SW, with $20 \pm 4\%$ of the energy delivered to the exploding wire being transferred to the generated water flow.

In this paper, we describe the results of experiments on the generation of toroidal SW using underwater electrical explosion of ring-shaped wire. It was found that the toroidal SW keeps its azimuthal symmetry during the main part of its convergence and that the convergence of the SW does not lead to an increase in the pressure at the SW front.

II. EXPERIMENTAL SETUP

A high-current generator based on a 4-stage Marx generator and water forming line^{10,11} with output current amplitude up to 50 kA and rise time of 70 ns was used in these experiments. The waveforms of the current $I(t)$ at the output

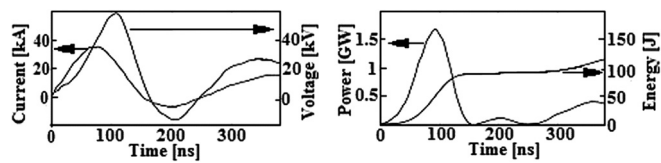


FIG. 1. (a) Waveforms of the discharge currents and resistive voltages; (b) power and deposited energy into the ring-shaped wires.

of the exploding wire and the voltage $\varphi_m(t)$ at the wire-cathode holder were measured using a current viewing resistor and capacitive voltage divider, respectively, and registered using a Tektronix TDS-784 A oscilloscope (see Fig. 1(a)). The energy deposited into the ring shape wires $W = \int_0^t I(t)\varphi(t)dt$ was ~ 100 J within the first 150 ns of the current pulse; a power of 1.7 GW was obtained (see Fig. 1(b)). Here, $\varphi(t) = \varphi_m(t) - Ldi(t)/dt$ is the resistive voltage, where L is the inductance of the wire cathode holder, which was determined in experiments with a short-circuit of the cathode-anode gap. Several shots with different wire diameters were made in order to find the diameter with the optimal energy deposition.

The loads in the experiments were two half-ring-shaped copper wires with a diameter of $100\mu\text{m}$ (see Fig. 2). The wires were stretched around a plastic cylinder placed between two cone-shaped stainless steel holders, through a 1 mm hole at the axis of each electrode. Each wire's end was soldered to the opposite side of the cone-shaped electrode, and then the plastic cylinder was removed, thus leaving a ring-shaped wire configuration. The diameter of this "ring" configuration was 20 mm.

The BNC 575 pulse delay generator was used to synchronize the operation of the high-current generator with the optical setup, which consisted of a pulsed laser, CCD cameras, and a fast framing intensified 4QuikE camera. The inner area of the exploded ring-shaped wire was back-lighted by either a 532-nm, 100 mW CW laser, and the captured images were recorded with the 4QuikE camera with an exposure time of ~ 5 ns, or by 532 nm, 5 ns Ekspla NL301G laser with images recorded by Canon EOS 450 and Nikon D60 CCD cameras with resolutions of 4272×2848 and 3872×2592 pixels, respectively. The 4QuikE camera operated in multi-frame mode with 600 ns time delays between

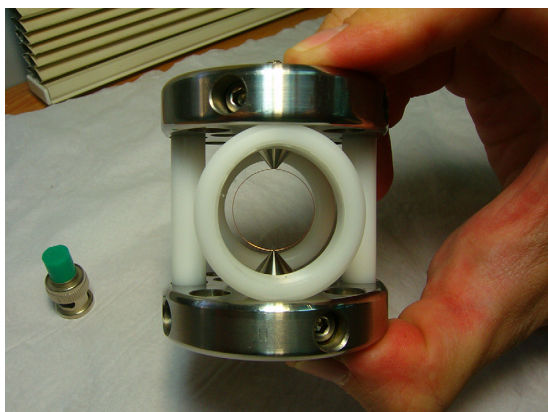


FIG. 2. Image of ring holder with a ring-shaped wire. The ring's diameter is 20 mm; it is made of Cu wire with a diameter of $100\mu\text{m}$.

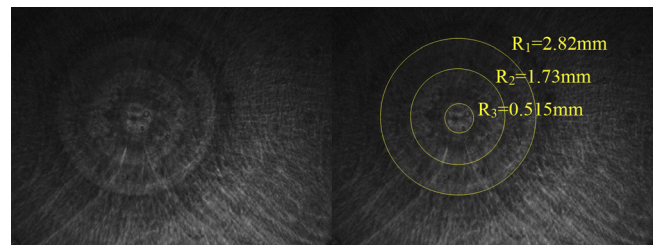


FIG. 3. Overlaid multi-frame image from the 4QuikE fast framing camera of the TOF experiments. Left—original image, right—same image with SW fronts marked for brevity, with the distances from the implosion axis.

the frames. A typical shadow image of three exposures of the propagating SW front, obtained at different time delays, is shown in Fig. 3. The CCD cameras were configured to operate either for shadowgraph or in a Schlieren setup. In some experiments, both configurations were used, and the image was split using a beam splitter (see optical schemes shown in Fig. 4).

In order to capture the dynamics of the annular underwater electrical wire explosion (UEWE), different magnifications of the optical setup were used, namely, 1:1 and 1:5, depending on the desired time delay and position of the converging SW. The 1:5 magnification was used to obtain the SW front in the vicinity $r \leq 1$ mm of the implosion. In this case, the space resolution was $\sim 20\mu\text{m}$, limited by the pixel dimension, which was $6\mu\text{m}$; around 3 pixels were needed to determine the front of the SW.

A crucial issue in these experiments was the alignment of the ring with the optical axis of the back-lighting laser, in order to avoid skewing of the SW front's shape, especially in the vicinity of the implosion. Even a slight misalignment caused the SSW image to become skewed, resulting in an artificially elliptic image (see Fig. 5) instead of a circular image of the radially converging shock wave. Therefore, an

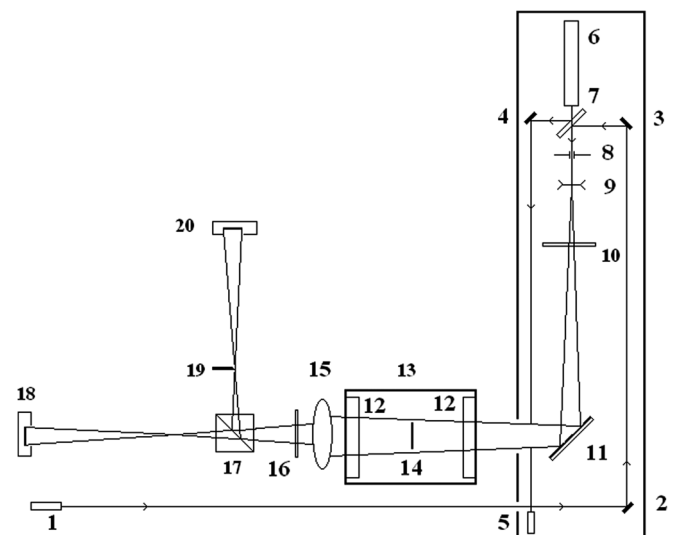


FIG. 4. Optical setup for simultaneous shadow and Schlieren imaging. 1—CW 532 nm dc laser; 2,3,4—1 in. flat mirrors; 5—photodetector; 6—pulsed 532-nm laser; 7—transparent parallel plate; 8—diaphragm; 9—negative lens; 10—ND filter; 11—2 in. flat mirrors; 12—windows in the experimental chamber; 13—experimental chamber; 14—load (straight wire or wire-ring); 15—objective lenses; 16—narrowband filter (full width at half height is 10 nm); 17—beam-splitter; 18—Canon CCD camera; 19—knife; 20—Nikon D60 CCD camera.

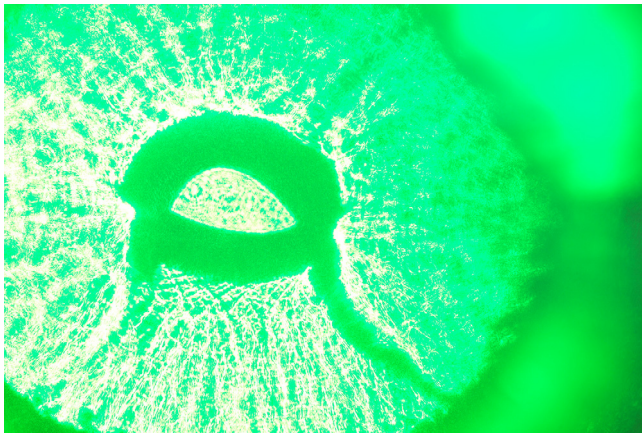


FIG. 5. A sample image of an annular SW in a misaligned optical configuration, taken by a CCD camera body.

additional backlighting optical scheme was used, which ensured the correct alignment of the ring-shaped wire plane with the back-lighting laser beam with an accuracy of $\sim 0.2^\circ$.

III. RESULTS

The shadow images of the annular SW (perpendicular to the plane of the ring), obtained by 4QuikE and CCD cameras, were used for the time-of-flight (TOF) analysis and the analysis of the shape of the converging SW front. The examples of simultaneously obtained shadow and Schlieren images of the annular SW at $r = 200 \mu\text{m}$ are shown in Fig. 6. These images, acquired with 1:1 magnification, have four noticeable regions. The undisturbed water at the center of the frame, denoted as “1,” is the region where the SW has not yet arrived.

The dark “circle,” marked by “2,” is the SW front and the region with compressed water immediately behind it. The density of water is related to the refraction index by the Gladstone-Dale relation¹² $n(r) = 1.332 + 0.332(\rho(r) - \rho_0)$; the refraction index is $n > 1.33$. This variation of density causes scattering and deflection of the back-lighting rays in this region of compressed water and prevents the rays from reaching the CCD sensor. The semi-transparent area, denoted by “3,” is the region of the water flow behind the SW. Here, the water density is lower than in region “2,” and the back-lighting rays pass through relatively undisturbed water. The area denoted by “4” is the region of the expanding Cu wire,

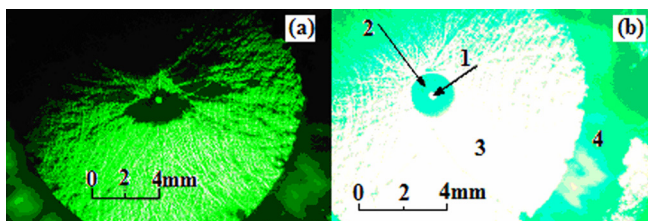


FIG. 6. Schlieren (a) and shadow (b) images of the imploding annular SW obtained with CCD cameras. The images were taken simultaneously at $t = 5.21 \mu\text{s}$, with zoom $\sim 1:1$. The radius of the undisturbed water is $R_w = 200 \mu\text{m}$. 1—undisturbed water area; 2—the shock wave front region with the highest refraction index; 3—water flow behind the shock wave; 4—expanded plasma channel of the exploded wire material.

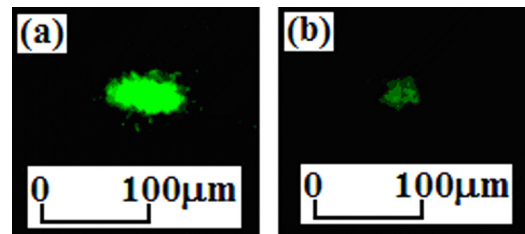


FIG. 7. Zoomed ($\sim 1:5$) shadow images of an imploding annular SW. (a) Elliptical form with large and small radii of ~ 40 and $\sim 25 \mu\text{m}$, respectively; (b) non-uniform front of the SW at radius of $\sim 17 \mu\text{m}$.

which is seen best in the Schlieren image (the dark circular area at the edges of this image). Images obtained by CCD camera with a magnification of 1:5 showed that the SW front retains its circular shape for almost the entire convergence process, i.e., $r \geq 50 \mu\text{m}$, with a sharp boundary between the SW and the undisturbed water. Thus, these experiments showed that a converging SW keeps its azimuthal symmetry up to compression factor of 100. At the smaller radii, the sharp boundary of the SW is clearly seen down to a radius of $r \geq 25 \mu\text{m}$; however, the form of the SW becomes elliptical (see Fig. 7(a)). The difference in the large and small radii of the elliptical structure of the SW front at these radii reaches $30 \mu\text{m}$. Here, let us note that an inaccuracy in the alignment of the wire ring plane perpendicular to the laser beam of $\sim 0.1^\circ$ could lead to the elliptical form of the front of the SW that was obtained at those radii. Finally, in Fig. 7(b), one can see the shadow image of the SW at the smallest radius of $\sim 15 \mu\text{m}$ obtained in these experiments. This image shows azimuthal irregularities, which strongly indicate the appearance of an azimuthal instability of the SW in the vicinity of the implosion.

The TOF data of the converging SW propagation are shown in Fig. 8. One can see the linear dependence of the SW front radius on time for $50 \mu\text{m} \leq r \leq 5000 \mu\text{m}$. The deduced velocity of the SW convergence is $V_C = 1.2M$, with an 2σ standard deviation of $< 1.5\%$ and an adjusted R^2 of 0.995, where M is the Mach number. This is rather an unexpected result, since in the case of gas, the convergence velocity of the SW grows as the radius becomes smaller.^{8,13}

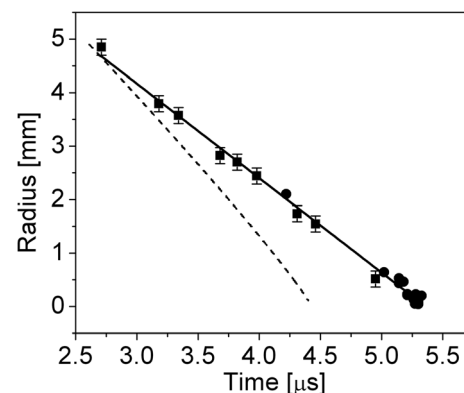


FIG. 8. Measurements of the radius of the annular shock wave front as a function of time. The data are incorporated from both the 4Quik fast framing camera (squares) and the CCD camera images (circles). The typical error of the 4Quik camera images is $150 \mu\text{m}$, and $5 \mu\text{m}$ of the CCD images. The dashed curve is the result of a calculation based on the acoustic approximation.¹⁴

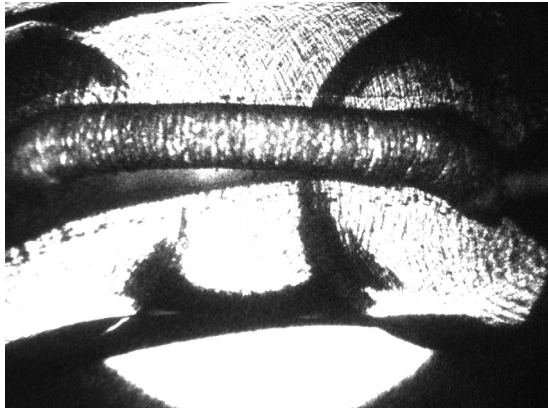


FIG. 9. Side-view 1:1 shadow image of an imploding annular SW at time delay of $t = 4 \mu\text{s}$ with respect to the beginning of the discharge current.

Finally, in Fig. 9, one can see the “side-view” image of the annular SW, obtained by the 4QuikE camera. The expanding plasma channel of the exploded wire is clearly seen at the center of the image. The semi-transparent annular SW is also seen, with its converging part at the center, partially blocked by the expanding wire material. The SW’s outer parts are clearly visible at the top and the bottom of the image. The inner SW front is also visible (especially the right one), as a circular dark curve.

IV. DISCUSSION

Let us discuss the peculiar result of these experiments, i.e., the fact that the converging annular SW propagating in water is imploding with a constant velocity of $\sim 1.2M$. First, we consider the hydrodynamic parameters of the Toroidal Shock Wave (TSW). The Mach number in the present experiment is relatively low, and therefore, one can use the equation-of-state for water¹²

$$P(\delta) \approx \frac{\rho_0 c^2}{\gamma} [\delta^\gamma - 1], \quad (1)$$

where $\delta = \rho/\rho_0$ is the dimensionless density and $\gamma \approx 7.15$ is the adiabatic coefficient of water. The constants used for this expression are $\rho_0 = 1 \text{ g/cm}^3$ and $c \approx 1.5 \times 10^5 \text{ cm/s}$, which are the density and speed of sound in water under normal conditions, respectively. For simplicity, let us assume a plane wave propagating with a velocity of $1.2M$. The corresponding density would be $\delta \approx 1.1$, and, respectively, the pressure would be $P \approx 3 \times 10^8 \text{ Pa}$. If this pressure rose to twice this

value, the value of δ would increase to $\delta \approx 1.3$ and the SW velocity would increase to $M \approx 1.5$. Such a rise in the velocity of the SW would have manifested itself in TOF measurements, and it did not.

An estimation of the distribution of the pressure in the acoustic approximation ($M = 1$) inside the weak SW was performed following Zel’dovich model.¹⁴ In our case, the toroidal SW was described as a superposition of many spherical waves, whose origins are distributed along the ring’s length. The obtained evolution of the pressure behind the front of the SW in the plane of the ring was approximated as $P_f(r) = P_R(R/r)^{0.33}$, where P_R is the known value of the pressure at radius R . Using this scaling law and the equation-of-state of water (Eq. (1)), the trajectory of the SW front was calculated and can be seen as dashed curve in Fig. 8. One can see that this trajectory does not coincide with the measured data points. Let us note that if the exponent in this scaling law will be modified in order to satisfactorily fit the experimental data, the result would be a mere 0.09, i.e., practically no cumulation at all. Therefore, a different model for the interpretation of this data is required.

Another possible case of a converging TSW was considered by Sokolov¹⁶ and Khudyakov.¹⁹ In the review by Sokolov,¹⁶ it was shown that if $R_C \gg r_f$, the inner part of the TSW looks like a cylindrically converging SW. Here, R_C is the radius of the SW in the roz plane, and r_f is the radius in the ring’s plane (see Fig. 10). Such cylindrically converging SW in water is characterized by an accompanying cumulation,³ which was not observed in the present experiment. Thus, in order to explain the measured data, one has to suppose that in the case of a TSW convergence in water the condition should be $R_C \sim r_f$.

Now we discuss the profile of the inner part of the TSW: in the “side-view” image of the underwater ring-shaped wire explosion (Fig. 9), the inward-looking part of the annular SW front looks circular. However, it is impossible to observe the inner-most part of the SW, because it is blocked by the expanding wire material. This “inward-looking” part of the TSW propagating toward the center with a constant implosion velocity of $\sim 1.2M$, which we will call from now on “the leading part of the annular SW,” is the cross-section area shown in Figs. 3, 5–7. The leading part of the SW is occupying a “patch” on the inner part of a torus. Each point at this patch is characterized by two mutually orthogonal radii of curvature: a convex one in the $ro\phi$ plane of the ring and a concave one in the roz plane (see Fig. 10).

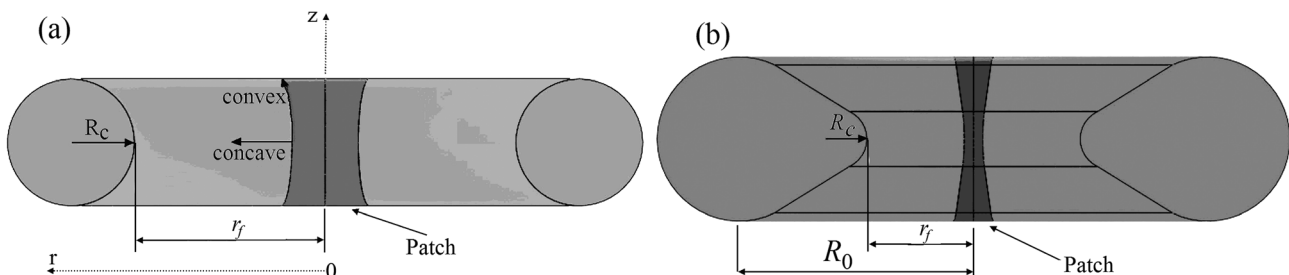


FIG. 10. Out-of-scale schematics of annular SW in water. (a) TSW at some early time. The arrows show the principal directions of the curvatures. (b) TSW during the “leading edge” development, when the radius of its convex curvature is not equal to its width. On both images—the transformation of a dark surface element during the TSW convergence.

Here, let us note that the value of r_f was experimentally measured, as opposed to the other radius R_C , which cannot be measured directly. In simple cylindrical or spherical geometry, the curvature K is defined as the reciprocal of the radius. For more complex surfaces, the average curvature $K = (1/r_1) + (1/r_2)$ is used,¹⁵ where r_1 and r_2 are called the principal radii of the curvature of the surface. In the case of a torus, the sign of one radius must be changed since the surface is both convex and concave, and therefore, the expression for the average curvature becomes $K = (1/r_1) - (1/r_2)$, which in our case is $K = (1/r_f) - (1/R_C)$.

In the case of a self-similar cylindrical implosion of the SW, the Mach number changes as $dM/dr \sim r^{-n}$,¹⁷ where n is the self-similarity parameter. In our case, we can use the averaged curvature of the torus K instead of the cylindrical one, and obtain the condition $dM/dr = \text{const}$, which implies convergence with a constant velocity, exactly as observed. An intuitive explanation for this phenomenon is as follows. The energy of an SW is distributed over the surface of its front. In the cylindrical and spherical cases, a surface element becomes smaller as the wave converges, which leads to an increase in the energy density and, respectively, cumulation is achieved. In the annular SW, the “inward-looking” surface element constantly changes its shape: at the beginning the element is wide and short (see Fig. 10(a)), whereas during the convergence it becomes narrow and long (see Fig. 10(b)). In terms of concentration of energy, if the surface area of this element becomes smaller, the energy density rises and *vice versa*. If, however, the ratio R_C/r_f is kept constant, the surface element indeed changes its shape, but its area remains constant, and therefore the energy density does not change during the convergence, and no cumulation is obtained.

Now, we consider a model of the leading part of the TSW wave front, propagating toward the center. The radii of curvature of this TSW front in the roz and $ro\phi$ planes are $R_C \sim r_f$ (see Fig. 11). The TSW front profile is a curved line in the roz plane, starting at the foremost point r_f on the r coordinate. A tangent plane can be placed at each point on this curve; therefore, the TSW front can be represented as a series of oblique SWs, whose inclination relative to the or axis gradually decreases. In order to analyze the dynamics of each such oblique SW element, it is convenient to work in a coordinate system moving with the SW front.^{6,18} In these coordinates, the undisturbed water velocity is U_{sw} along the r axis, and β is the angle between the SW and this velocity.

The velocity of the water behind the front is U_1 (the “out-flowing” water), and its angle with respect to the axis r is α . An analysis of an oblique SW (see Ref. 18) shows that the pressure of the SW is $P_{sw} = \rho_0 U_{sw}^2 (\sin \beta)^2 (\delta - 1) / \delta$, and the relations between the angles and the hydrodynamic parameters are

$$\begin{aligned} ctg^2 \beta &= \frac{\rho_0 U_{sw}^2}{P_{sw}} \frac{\delta - 1}{\delta} - 1; \\ t g \alpha &= \sqrt{\frac{P_{sw}}{\rho_0 U_{sw}^2} \left(\frac{\delta - 1}{\delta} - \frac{P_{sw}}{\rho_0 U_{sw}^2} \right)} \left(1 - \frac{P_{sw}}{\rho_0 U_{sw}^2} \right)^{-1}. \end{aligned} \quad (2)$$

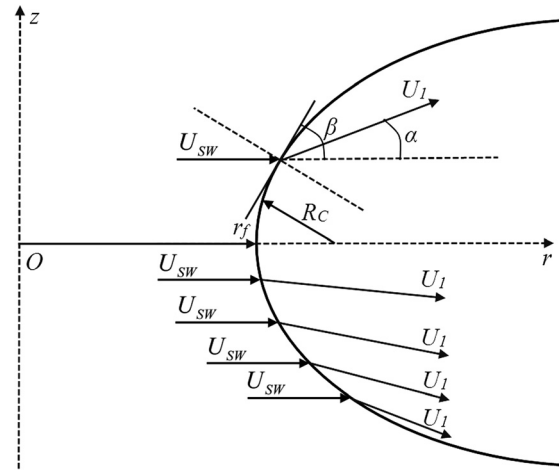


FIG. 11. Cross-section of the leading part of the TSW in the roz plane. Note the fanning-out of the water flow as it passes through the TSW front. A symmetric fanning-out is obtained in the upper part.

In the case of an SW propagating in water, the distribution of the pressure behind the SW front $P(\delta)$ is given by Eq. (1). We rewrite Eqs. (2) using the Mach number notation ($M = U_{sw}/c$)

$$\begin{aligned} ctg^2 \beta &= \gamma M^2 \left(\frac{\delta - 1}{\delta(\delta^\gamma - 1)} \right) - 1; \\ t g \alpha &= \sqrt{\frac{\delta - 1}{\delta} \frac{\gamma M^2}{(\delta^\gamma - 1)} - 1} \left(\frac{\gamma M^2}{\delta^\gamma - 1} - 1 \right)^{-1}. \end{aligned} \quad (3)$$

Let us note that at the limit $\beta \rightarrow \pi/2$, the oblique SW is transformed back into a straight SW propagating with $M = \sqrt{\delta(\delta^\gamma - 1) / [\gamma(\delta - 1)]}$. At the leading part of the SW front, $r = r_f = Mct$. Now let us consider a point at the SW front with $r \geq r_f$. In this case, one obtains a slight decrease in the angle β and a slight decrease in $\delta(r)$ as compared with $\delta(r_f) \equiv \delta_f$ due to divergence of the water flow behind the SW front. We note that $t g \beta = dz/dr$, i.e., one can consider Eq. (3) as the equation for the shape of the leading part of the SW at small deviations of the angle β from $\pi/2$. The main interest is in the curvature K as the SW propagates toward the center of the ring. By using this definition and by taking another derivative by r of Eq. (3), one can find the desired dependence between the curvature K and the dimensionless density. Eq. (3) can be re-written as

$$t g \beta = \frac{dz}{dr} = F(\delta), \quad F(\delta) \equiv \left(\gamma M^2 \left(\frac{\delta - 1}{\delta(\delta^\gamma - 1)} \right) - 1 \right)^{-0.5}. \quad (4)$$

Now, one obtains the differential equation

$$\begin{aligned} \frac{d^2 z}{dr^2} &= -\frac{F^3(\delta)}{2} \frac{dF^2(\delta)}{d\delta} \frac{d\delta}{dr}, \\ \frac{dF(\delta)}{d\delta} &\equiv \gamma M^2 \left(\frac{(\delta^\gamma - 1) - (\delta - 1)\gamma\delta^\gamma}{\delta^2(\delta^\gamma - 1)^2} \right) \frac{d\delta}{dr}. \end{aligned} \quad (5)$$

Substitution of Eq. (5) into the above mentioned definition of curvature gives

$$K(r) = \frac{F^3(\delta)}{2[1 + F^2(\delta)]^{3/2}} \left[\frac{dF^{-2}(\delta)}{d\delta} \right] \frac{d\delta}{dr}. \quad (6)$$

Now let us find the solution of Eq. (6) for angles $\beta \rightarrow \pi/2$, i.e., near the point r_f . Noting that $F(\delta_f) \rightarrow \infty$, since $\operatorname{tg}(\pi/2) \rightarrow \infty$, one obtains that $\frac{F^3(\delta)}{[1 + F^2(\delta)]^{3/2}} \sim 1$, and therefore, $K(r)$ is reduced to

$$K(r) = B \frac{d\delta}{dr}, \quad B \equiv -\frac{1}{2} \left| \frac{dF^{-2}(\delta)}{d\delta} \right|_{\delta=\delta_f}. \quad (7)$$

Now we set the condition that the radius of the curvature of the leading front of the SW in the roz plane is $R_C \approx r_f$, which allows finding the distribution of $\delta(r)$ at the leading front of the SW by using the condition $K = 1/r_f$ and Eq. (7)

$$\delta(r) \approx \delta_f - (1/|B|) \ln(r/r_f). \quad (8)$$

This solution provides the distribution of the water density in the proximity of the leading edge of the SW front, i.e., where $r_f \gg r - r_f$. Using known value of M , one can compute the numerical value of δ_f and, using Eqs. (7) and (8), the value of parameter B and of $d\delta/dr$, respectively. Substituting these values and the experimental convergence velocity into the EOS of water in Eq. (1), one can reconstruct the pressure at the front of the SW in that region: at the radius close to the leading edge $r \rightarrow r_f$, the compression of water is $\delta_f \approx 1.13$, and the value of the parameter $B \approx 4.04$. As one moves along the SW front $r > r_f$, the compression value $\delta(r)$ decreases, the pressure behind the SW front $P(\delta)$ decreases, and so does the angle β of the oblique SW. The shape of the SW (at the roz plane) at different distances from the z axis, obtained as solution of Eqs. (4) and (8), is shown in Fig. 12. One can see that the radius of the curvature of the SW front is equal to its distance from the center ($r = r_f$) and the curvature slowly decreases for $r > r_f$.

Now, using the solution near the leading part of the SW, one can consider a qualitative explanation of the lack of cumulation in the annular geometry: the flux of the water passing through the SW front is deflected at various angles α with respect to the r axis, and then the water flow behind the

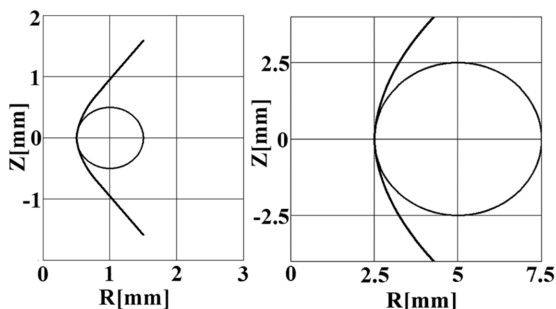


FIG. 12. Annular SW cross-sections at different times prior to implosion: left— $t \sim 300$ ns; right— $t \sim 1400$ ns. The circles denote the shock wave's curvature.

SW front fans out across the z axis. Thus, despite the attempt to cumulate the pressure in the plane of the ring ($ro\varphi$) at the point r_f , the spread of the water flow in the perpendicular direction (roz plane) effectively unloads the excessive pressure and allows it to re-distribute itself along the front in the z direction. In other words, the SW is cumulating in the ring's plane and is decaying in the perpendicular plane; these competing processes prevent cumulation on the one hand, but on the other also do not allow the complete decay of the SW; hence, one obtains the constant implosion velocity of the annular SW in water.

V. SUMMARY

Experimental results of nanosecond time-scale underwater electrical explosions of ring-shaped wires are presented. The dynamics of the resulting annular SW in water is evaluated in a wide range of radii. It is shown that the leading part of the SW front maintains its circular shape up to radii of $50 \mu\text{m}$ (a convergence factor of 100). At smaller radii $r \leq 15 \mu\text{m}$, azimuthal irregularities of the SW front were obtained, which manifest the appearance of azimuthal instability of the SW in the vicinity of its implosion. Time-of-flight measurements show that the annular SW maintains a constant implosion velocity. No cumulation of the hydrodynamic parameters of water is observed; however, the decay of the implosion velocity is not observed either. The presented model, based on the oblique SW front description, coupled with the condition of the approximate equality of the characteristic radii of the annular geometry, $R_C \sim r_f$, and constant implosion velocity, provides a plausible explanation for the absence of cumulation. **Acknowledgments:**

This research was supported by the Center for Absorption in Science, Ministry of Immigrant Absorption, State of Israel.

- ¹E. I. Zababahin, *Sov. Phys. Usp.* **8**, 295 (1965).
- ²I. V. Sokolov, *Sov. Phys. Usp.* **33**, 960 (1990).
- ³A. Fedotov-Gefen, S. Efimov, L. Gilburd, G. Bazalitski, V. Tz. Gurovich, and Ya. E. Krasik, *Phys. Plasmas* **18**, 062701 (2011).
- ⁴K. V. Brushlinskii and Ya. M. Kazhdan, *Rus. Math. Surv.* **18**, 1 (1963).
- ⁵G. Guderley, *Luftfahrtforschung* **19**, 302 (1942).
- ⁶L. D. Landau and E. M. Lifshitz, *Fluid Mechanics*, 2nd ed. (Butterworth-Heinemann, Oxford, 1987).
- ⁷K. P. Stanyukovich, *Unsteady Motion of Continuous Media* (Pergamon Press, NY, 1960).
- ⁸N. K. Berezhtskaya, E. F. Bol'shakov, S. K. Golubev, A. A. Dorofeyuk, I. A. Kossyi, V. E. Semenov, and V. E. Terekhin, *Sov. Phys. JETP* **60**, 6 (1984).
- ⁹D. Sheftman and Ya. E. Krasik, *Phys. Plasmas* **18**, 092704 (2011).
- ¹⁰D. Sheftman and Ya. E. Krasik, *Phys. Plasmas* **17**, 112702 (2010).
- ¹¹A. Grinenko, Ya. E. Krasik, S. Efimov, V. Tz. Gurovich, and V. I. Oreshkin, *Phys. Plasmas* **13**, 042701 (2006).
- ¹²M. A. Harith, V. Palleschi, A. Salvetti, M. Vaselli, E. M. Barkudarov, M. O. Mdivnishvili, and M. Taktakishvili, *J. Phys. D* **22**, 1451 (1989).
- ¹³Ya. B. Zel'dovich and Yu. P. Raizer, *Physics of Shock Waves and High-Temperature Hydrodynamic Phenomena* (Academic Press, NY, 1966).
- ¹⁴Ya. B. Zel'dovich, "Cylindrical self-similar acoustic waves," *Zh. Eksp. Teor. Fiz.* **3**, 9 (1957).
- ¹⁵G. A. Korn and T. M. Korn, *Mathematical Handbook* (McGraw-Hill, NY, 1968).
- ¹⁶I. V. Sokolov, *Sov. Phys. JETP* **64**, 4 (1986).
- ¹⁷G. B. Witham, *Linear and Nonlinear Waves* (John Wiley and Sons, NY, 1974).
- ¹⁸E. I. Zababahin, *Some Aspects of Explosion Gas Dynamics* (RFNC-VNIITF, Snezhinsk, 1997).
- ¹⁹V. M. Khudyakov, *Sov. Phys. Doklady* **31**, 298 (1986).